Influence of Upper-Troposphere Stratification and Cloud–Radiation Interaction on **Convective Overshoots in the Tropical Tropopause Layer**

Zeyuan Hu,^a Fayçal Lamraoui,^a and Zhiming Kuang^{a,b}

^a Department of Earth and Planetary Sciences, Harvard University, Cambridge, Massachusetts ^b John A. Paulson School of Engineering and Applied Sciences, Harvard University, Cambridge, Massachusetts

(Manuscript received 10 August 2020, in final form 12 May 2021)

ABSTRACT: It is still debated whether radiative heating observed in the tropical tropopause layer (TTL) is balanced primarily by cooling from convective overshoots, as in an entrainment layer, or by adiabatic cooling from large-scale eddydriven upwelling. In this study, three-dimensional cloud-resolving model simulations of radiative-convective equilibrium were carried out with three different cloud microphysics schemes and 1-km horizontal resolution. We demonstrate that overshooting cooling in the TTL can be strongly modulated by upper-troposphere stratification. Two of the schemes produce a hard-landing scenario in which convective overshoots reach the TTL with frequent large vertical velocity leading to strong overshooting cooling (\sim -0.2 K day⁻¹). The third scheme produces a soft-landing scenario in which convective overshoots rarely reach the TTL with large vertical velocity and produce little overshooting cooling ($\sim -0.03 \, \mathrm{K} \, \mathrm{day}^{-1}$). The difference between the two scenarios is attributed to changes in the upper-troposphere stratification related to different atmospheric cloud radiative effects (ACRE). The microphysics scheme that produces the soft-landing scenario has much stronger ACRE in the upper troposphere leading to a ~3-K-warmer and more stable layer that acts as a buffer zone to slow down the convective updrafts. The stratification mechanism suggests the possibility for the ozone variation or eddy-driven upwelling in the TTL to modulate convective overshoots. We further test the sensitivity of overshooting cooling to changes in model resolution by increasing the horizontal resolution to 100 m. The corresponding change of overshooting cooling is much smaller compared with the difference between the hard-landing and soft-landing scenarios.

KEYWORDS: Deep convection; Tropopause; Cloud radiative effects

1. Introduction

The tropical tropopause layer (TTL), which is located approximately between 14 and 18.5 km, is a gradual transition layer between tropical troposphere and stratosphere (e.g., Fueglistaler et al. 2009; Randel and Jensen 2013), and the air enters the stratosphere in the tropics through the TTL (e.g., Brewer 1949; Holton et al. 1995). The associated dehydration processes in the TTL (e.g., freeze-drying as air passes the coldpoint tropopause) are of critical importance on the global stratospheric water vapor content (e.g., Mote et al. 1996; Holton et al. 1995; Randel and Park 2019). Changes in stratospheric water vapor can substantially influence ozone chemistry, stratospheric radiation, and even tropospheric climate (e.g., Anderson et al. 2017; Dessler et al. 2013). Atmospheric properties such as lapse rate, heat balance, and circulation pattern gradually transit through the TTL from their tropospheric to stratospheric characteristics. From the perspective of the heat budget, the dominant process in the troposphere is convection that balances tropospheric negative radiative heating predominantly through the latent heat release. In the stratosphere, the adiabatic cooling associated with the ascent of the eddy-driven Brewer-Dobson circulation (e.g., Butchart 2014) balances the radiative heating. In the TTL, both deep convection and eddy-driven circulation could contribute to balancing the observed radiative heating (e.g., Fueglistaler et al. 2009). The relative importance of deep convection and eddy driven circulation in the

heat balance is still unclear in the TTL (e.g., Fueglistaler et al. 2009; Lin et al. 2017). Two main processes related to deep convection have been

proposed to balance the radiative heating in the TTL. The first process is the diabatic, irreversible mixing between convective overshoots and the environment. Since the convective overshoots above their levels of neutral buoyancy are negatively buoyant, the irreversible mixing of colder overshooting air with the warmer environment causes a downward buoyancy flux in the TTL (Kuang and Bretherton 2004; Robinson and Sherwood 2006; Hartmann et al. 2019), as in an entrainment layer (Deardorff et al. 1980), capping the turbulently mixed troposphere below. At high altitudes in the upper limit of deep convection, the buoyancy flux fades out and the resulting divergence leads to cooling in the TTL. The second process is the adiabatic ascent in response to the convective heating in the upper troposphere. Sherwood et al. (2003) found that adiabatic ascent contributes partly to the TTL cooling above convective systems, which is further supported by numerical simulations in Robinson and Sherwood (2006). Holloway and Neelin (2007) showed that adiabatic ascent could be a hydrostatic adjustment of the large-scale circulation in response to convective heating and high pressure at the upper troposphere.

On the other hand, large-scale eddy-driven upwelling also substantially influences the TTL thermal structure. The annual cycle of tropopause temperature is mainly related to the annual cycle of the adiabatic upwelling (e.g., Jucker and Gerber 2017; Yulaeva et al. 1994), while the radiative effect associated with the change of ozone and water vapor also plays a role (Ming et al. 2017). The residual-mean upwelling velocity in the TTL

Corresponding author: Zeyuan Hu, zeyuan_hu@fas.harvard.edu

estimated from different reanalysis data (Kobayashi and Iwasaki 2016; Yoshida et al. 2018) is on the same order as the upwelling velocity needed to balance the observed TTL radiative heating (Yang et al. 2008). However, certain discrepancies in upwelling velocity exists between different reanalysis data. It is an ongoing debate whether the observed negative radiative heating rate in the TTL is balanced primarily by cooling from convective overshoots or by adiabatic cooling from hydrostatic adjustment to tropospheric heating and/or large-scale eddy-driven upwelling.

Near-global cloud-resolving simulations (e.g., Bretherton and Khairoutdinov 2015; Stevens et al. 2019) that resolve both deep convection and eddy-driven circulation may provide compelling results of the TTL heat budget. However, this type of simulation has just become possible in recent years due to increasing computational power. To our knowledge, such global high-resolution simulations have not yet been designed to study the TTL, which generally needs high vertical resolution near the TTL to prevent artificial wave breaking (e.g., Kuang and Bretherton 2004; Kobokawa et al. 2012). Before running these computationally expensive runs, it is important to understand whether the processes in the TTL could be sensitive to certain experimental settings. Some previous studies involving 3D small-domain cloud-resolving simulations (e.g., Kuang and Bretherton 2004; Robinson and Sherwood 2006) found significant cooling related to convective overshoots in the TTL, while Küpper et al. (2004) did not. Hereafter, we will simply use the term "convective cooling" to describe the cooling related to convective overshoots and irreversible mixing. It is proper in RCE simulations because domain-mean upwelling, and therefore the hydrostatic balance mechanism, is inhibited. Fueglistaler et al. (2009) argued that the convective cooling in the TTL could depend on the prescribed boundary conditions. In a 1D radiative-convective equilibrium (RCE) model with parameterized temperature tendency due to convection, Dacie et al. (2019) showed that the convective cooling could become weaker when the prescribed surface temperature is increased.

In this study, we ran small-domain RCE simulations in a 3D cloud-resolving model to examine what experimental settings could potentially influence the strength of convective cooling in the TTL. We found that cloud microphysics (i.e., the choice of microphysical scheme) can strongly influence the strength of convective overshoots through modifying the upper-troposphere stratification. Two microphysics schemes we used produce a hard-landing scenario in which convective overshoots reach the TTL with high velocity and relatively high frequency and lead to strong overshooting cooling $(\sim -0.2 \,\mathrm{K}\,\mathrm{day}^{-1})$ in the TTL. On the other hand, the third scheme produces a soft-landing scenario in which convective overshoots rarely reach the TTL with large velocity and produce little overshooting cooling (\sim -0.03 K day⁻¹) in the TTL. The microphysical scheme in the soft-landing scenario produces much stronger atmospheric cloud radiative effects (ACRE) leading to a ~3-K-warmer and more stable upper troposphere, which acts as a buffer zone to weaken convective updrafts. We will also demonstrate the implication of the microphysics dependence to the question of which processes dominate the heat budget in the TTL, although our experiments cannot directly address this question.

The rest of this paper is organized as follows: section 2 describes the experiment design. Section 3 shows the hardlanding and soft-landing scenarios of convective overshoots produced by the different cloud-microphysics schemes. Section 4 links the different strengths of convective overshoots to the difference in upper-troposphere stratification and ACRE. In section 5, we explore why the three microphysics schemes produce different ACRE. In section 6, we discuss our results. In section 6a, we discuss the influence of increasing model resolution from 1 km to 100 m on convective cooling. In section 6b, we discuss the heat balance in the TTL in hard-landing and soft-landing scenarios when a large-scale upwelling velocity is imposed to mimic eddy-driven upwelling in the TTL. In section 6c, we explore the possibility for ozone variation to modulate convective overshoots through modifying the upper-troposphere stratification. In section 7, we summarize the results.

2. Experiment setup

We use the System for Atmosphere Modeling (SAM; Khairoutdinov and Randall 2003), version 6.10.6, configured as a cloud-resolving model. We run three-dimensional RCE simulations using the same domain size of 64×64 grid points and 1-km horizontal grid spacing with periodic lateral boundary condition. All simulations use 170 vertical levels with model top located at 40 km and a rigid-lid top boundary condition. The vertical grid spacing increases from 50 m near the surface to 500 m at the midtroposphere and then decreases to reach 100 m near the TTL between 14.5 and 19.5 km. The small vertical grid spacing near the TTL is crucial to reducing numerical dissipation caused by artificial gravity wave breaking (e.g., Kuang and Bretherton 2004). A sponge layer is located in the upper 30% of the model domain (i.e., above 28 km). The radiation scheme is Rapid and Accurate Radiative Transfer Model for General Circulation Models (RRTMG) (Iacono et al. 2008). A simple Smagorinsky-type scheme (Khairoutdinov and Randall 2003) is used for the effect of subgrid-scale motion. We use a constant solar insolation (no diurnal cycle) with fixed solar constant of 683.5 W m⁻² and zenith angle of 50.5°. Domain-averaged horizontal wind is nudged to zero at each vertical level with a nudging time scale of 1 h. Sea surface temperature (SST) is fixed uniformly at 30.5°C. The ozone concentration profile is specified and cannot interact with convection (shown and discussed later in section 6c).

A set of three simulations was carried out with three different cloud-microphysics schemes: SAM single-moment scheme (SAM1MOM; Khairoutdinov and Randall 2003), a double-moment scheme (Morrison et al. 2005), and a hybrid one- and double-moment hydrometeor species (double-moment only for cloud ice and rain) scheme (Thompson et al. 2008). This set of three simulations is hereafter called the default set (DEFAULT), and the three simulations are called herein SAM1MOM_DFT, Morrison_DFT, and Thompson_DFT. Table 1 summarizes all the experiment sets that will be discussed later and illustrates the abbreviation of individual

TABLE 1. Summary of experiment setup for different sets of simulations.

Experiment set	Simulation abbreviation	Large-scale forcing	Radiation
DEFAULT	SAM1MOM_DFT Thompson_DFT Morrison_DFT	No forcing	Default RRTMG
Switch-profile	SAM1MOM_MORprl	Add tuned tendency of temperature and water vapor	Default RRTMG
	Morrison_SAMprl	Add tuned tendency of temperature and water vapor	
NOCRE	SAM1MOM_NOCRE	No forcing	No cloud radiative effect
	Thompson_NOCRE		No cloud radiative effect
	Morrison_NOCRE		No cloud radiative effect
	Morrison_NOCRESW		No SW cloud radiative effect
	Morrison_NOCRELW		No LW cloud radiative effect
100-m resolution	SAM1MOM_100m Morrison 100m	No forcing	Default RRTMG
BDC	SAM1MOM_BDC Thompson_BDC Morrison_BDC	W to mimic Brewer–Dobson circulation	Default RRTMG
OZONE	SAM1MOM_Feb SAM1MOM_Aug SAM1MOM_Aug+2	No forcing	ERA5 February ozone profile ERA5 August ozone profile ERA5 August ozone profile +2 mg kg ⁻¹ between 10 and 14 km

simulations and their different treatment of large-scale forcing and radiation.

Significant differences exist between the three microphysics schemes. For example, the SAM one-moment scheme uses an instantaneous supersaturation adjustment to generate cloud condensate. Between 0° and -20°C, partitioning of cloud condensate into cloud ice and liquid water depends linearly on temperature (at -20°C, all condensate is ice; at 0°C, all condensate is liquid water). More pathways for conversion between different hydrometeors are included in the Morrison and Thompson schemes (e.g., see Table 2 in Bao et al. 2019). The cloud ice tendency due to autoconversion from cloud ice to snow is more than 30 times faster in the Thompson scheme than in the Morrison scheme in the upper troposphere (see Fig. 8 in Bao et al. 2019). This fast autoconversion from cloud ice to snow can make anvil clouds dissipate faster in the Thompson scheme than in the Morrison scheme (e.g., Hartmann et al. 2018; Feng et al. 2018). Powell et al. (2012) argued that the Morrison scheme tends to overproduce ice cloud due to a large cap on ice number concentration (10 cm⁻³, two orders of magnitude larger than that in the Thompson scheme, 0.25 cm⁻³) and consequentially a slower sedimentation rate. Although the cap on ice number concentration in the Morrison scheme has been lowered (by model developers) to 0.3 cm⁻³ as the default value in the version of SAM model that we use, as we will show later, the Morrison scheme still produces much more cloud ice in the upper troposphere. We still do not have a complete understanding of why different microphysics schemes produce different cloud properties, for example, different cloud fraction and mixing ratio of different hydrometers. However, we take this uncertainty as a possible range for the realistic climate on Earth and explore how the convective overshoots in the TTL could behave differently within this range.

For all the simulations listed in Table 1, the first 100 days are abandoned for the model spinup and considered long enough to reach equilibrium. This 100-day period is the typical time determined by eye when the time series of domain-averaged temperature at any level below 16 km get flattened and do not exhibit a clear trend. The temperature at ~18 km still has a small trend that has little effect on the convective overshoots below. After the 100-day spinup, a 50-day postequilibrium period is used for most simulations. The domain-mean statistics are sampled every 2 min. The 30-samples-per-hour data are then averaged to get an hourly output of domainmean statistics. For the analysis period, the linear regression trend of temperature at any level below 16 km is on the order of 0.001 K day⁻¹ across all the simulations and is below 0.02 K day⁻¹ at 18 km. The DEFAULT simulations were run for 270 days to examine whether the temperature trend in the upper TTL can influence the results. Analyzing days 100-150 and 220-270 will not change the results in the following section. For the 100-m-resolution simulations in Table 1, only a 20-day postequilibrium period is used due to computational limitations. When we examine other simulations with a 50-day postequilibrium period, averaging over 20 days gets sufficiently similar and stable domain-mean statistics compared to that obtained from averaging over the full 50 days.

3. The dependence of convective overshoots on cloud microphysics

To compare the convective influence on TTL heat budget, we show the domain-averaged profiles of convective heating rate in Fig. 1a. The convective heating is calculated by reversing the sign of the radiative heating rate. As shown in Fig. 1a, both the SAM1MOM_DFT and Thompson_DFT

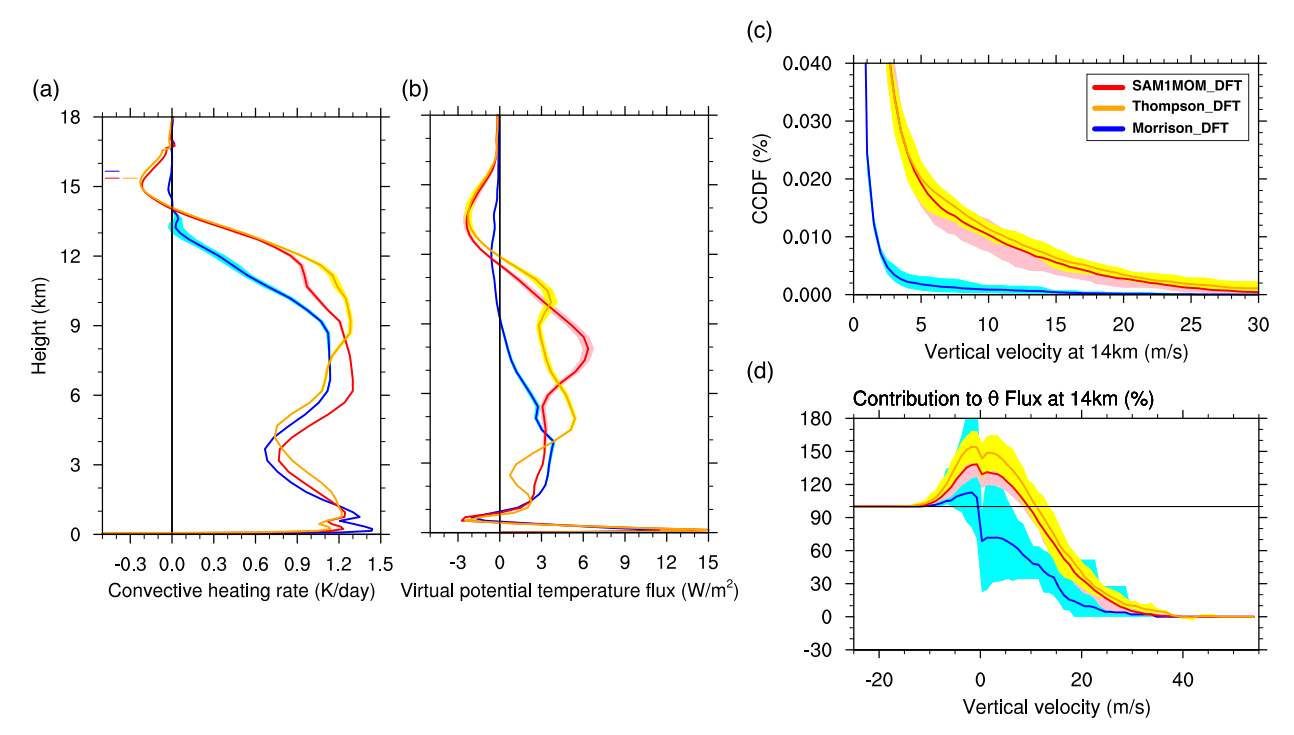


FIG. 1. Differences of convective overshoots in the DEFAULT set of simulations: SAM1MOM_DFT (red), Thompson_DFT (orange), and Morrison_DFT (blue). (a) Domain-averaged profiles of convective heating rate, calculated as the negative of the radiative heating rate. The short horizontal lines indicate the cold-point tropopause. (b) Domain-averaged profiles of virtual potential temperature flux $(\rho C_p \overline{w'\theta'_v})$. (c) The CCDF (similar to CDF but integrating from the largest sample value) of vertical velocity at 14 km. (d) Contribution of different vertical velocity to the virtual potential temperature flux at 14 km, defined as $Contr(W_0) = \sum_{w'>W_0} w'\theta'_v / \sum_{all\,w'} w'\theta'_v$. The shading in (a) and (b) indicates the 95% confidence interval. The shading in (c) and (d) indicates the range based on the five 10-day periods for a total of 50 days.

simulations show a convective cooling between 14 and 17 km with a minimum convective heating rate of \sim -0.2 K day⁻¹ at around 15 km. On the other hand, the Morrison_DFT simulation shows a weaker convective cooling in the TTL, with a minimum cooling rate of \sim -0.03 K day⁻¹ at around 15 km and near zero above 15.5 km.

In our way of defining the convective heating rate by reversing radiative heating rate, we assume that the temperature has reached equilibrium and all other nonconvective processes, such as subgrid-scale diffusion or gravity wave processes, are sufficiently small. As we mentioned in the previous section, the maximum temperature drift below 18 km across all the simulations listed in Table 1 is between 0.001 and 0.02 K day⁻¹. The maximum time-mean temperature tendency due to subgridscale diffusion in the TTL across all the simulations is between 0.001 and $0.015 \,\mathrm{K} \,\mathrm{day}^{-1}$. In the TTL, there is no direct temperature tendency related to the sponge layer, which is above 28 km. The temperature tendency associated with gravity wave processes, such as wave breaking and physical or numerical damping, is difficult to quantify accurately. However, we will show later in Fig. 1d that, at least for the SAM1MOM_DFT and Thompson_DFT simulations that have strong convective cooling, the resolved advective temperature tendency in the TTL is dominated by strong convective overshoots rather than gravity waves in the environment.

Consistent with convective cooling, the domain-averaged profile of virtual potential temperature flux shows a clear difference in the Morrison_DFT simulation compared to the other two DEFAULT simulations (Fig. 1b). Here, the virtual potential temperature flux $(\overline{w'\theta'_v})$ is expressed in the form of energy flux $(\rho C_p \overline{w' \theta'_v})$ with units W m⁻², where ρ is the air density, C_p is the specific heat capacity at constant pressure, w'is the perturbation in vertical velocity, and θ'_{v} is the perturbation in virtual potential temperature. The virtual potential temperature, $\theta_v = (1 + 0.61r - r_c)$, includes the effect of both water vapor mixing ratio r and the mixing ratio of total (precipitating plus nonprecipitating) cloud condensate r_c . Near the TTL, because the air is quite dry (both r and r_c are on the order of $10^{-5} \,\mathrm{kg} \,\mathrm{kg}^{-1}$), the virtual potential temperature flux profile shape is comparable to those of buoyancy flux and turbulent heat flux. For the SAM1MOM_DFT and Thompson_DFT simulations, the domain-mean level of neutral buoyancy (LNB, defined here as the level where the virtual potential temperature flux reaches zero) is near 12 km. The downward virtual potential temperature flux above the LNB is due to the temperature difference between colder convective overshoots and the warmer environment and the irreversible mixing between them. The virtual potential temperature flux reaches its minimum value at near 14 km, and the divergence of heat flux above leads to the convective cooling in Fig. 1a.

By comparison, the Morrison_DFT simulation generates lower LNB, which indicates that most of the convective updrafts lose their positive buoyancy at a much lower altitude of \sim 9 km. Furthermore, the corresponding minimum value of the negative virtual temperature flux above the LNB is very small, leading to a weaker heat flux divergence in the TTL.

The differences in the convective cooling in the TTL and the virtual potential temperature flux are associated with weaker convective overshoots (i.e., rare occurrence of strong updrafts at a given height) in the Morrison_DFT simulation. The complementary cumulative distribution function (CCDF) of the vertical velocity [i.e., CCDF $(w_0) = P (w > w_0)$, the probability of w greater than w_0] at 14 km is illustrated in Fig. 1c. To calculate the CCDF, we output the instantaneous hourly 3D vertical velocity field during the 50-day time period. At the level of ~14 km, the vertical velocity is sampled at each grid point. As shown in Fig. 1c, the Morrison_DFT simulation indicates an occurrence of strong updraft (e.g., greater than 10 m s⁻¹) one order of magnitude smaller than that in the other two DEFAULT simulations. The CCDF of the vertical velocity at 13 or 15 km also shows much rarer strong updraft in the Morrison_DFT simulation (not shown).

To illustrate which updraft velocity contributes most to the virtual potential temperature flux, we show in Fig. 1d the integrated contribution of different vertical velocities to the virtual potential temperature flux at 14km. The integrated contribution is defined as $Contr(W_0) = \sum_{w'>W_0} w'\theta'_v / \sum_{\text{all } w'} w'\theta'_v$. For the SAM1MOM_DFT and Thompson_DFT simulations, updraft velocities greater than ~10 m s⁻¹ contribute almost 100% to the total virtual potential temperature flux, while the contribution from updraft velocities smaller than 10 m s⁻¹ is roughly canceled out by downdrafts. Almost all updrafts that exceed 10 m s⁻¹ are related to convective overshoots originated from the boundary layer rather than gravity wave processes in the environment (which is supported by tracer analysis, not shown). In the Morrison_DFT simulation, updrafts greater than $10 \,\mathrm{m\,s^{-1}}$ only explain part of the total virtual potential temperature flux, while downdrafts smaller than about 1 m s⁻¹ also contributes a lot. For the contribution from small velocities, it is hard to cleanly separate convective overshoots and gravity wave processes. Therefore, convective overshoots dominate the virtual potential temperature flux at 14 km in the SAM1MOM_ DFT and Thompson_DFT simulations but could have a comparable contribution to gravity wave processes in the Morrison DFT simulation.

The difference between the convective overshoots in the SAM1MOM_DFT or Thompson_DFT simulations and those in the Morrison_DFT simulation may be viewed in terms of hard landing versus soft landing. In the hard-landing scenario (for the SAM1MOM_DFT and Thompson_DFT simulations), convective overshoots reach the TTL with frequent strong updrafts, leading to strong downward heat flux and a significant cooling in the TTL. In the soft-landing scenario (for the Morrison_DFT simulation), convective updrafts start to decelerate at lower heights and convective overshoots rarely reach the TTL with high vertical velocity, producing weak downward heat flux and little cooling in the TTL. In the next

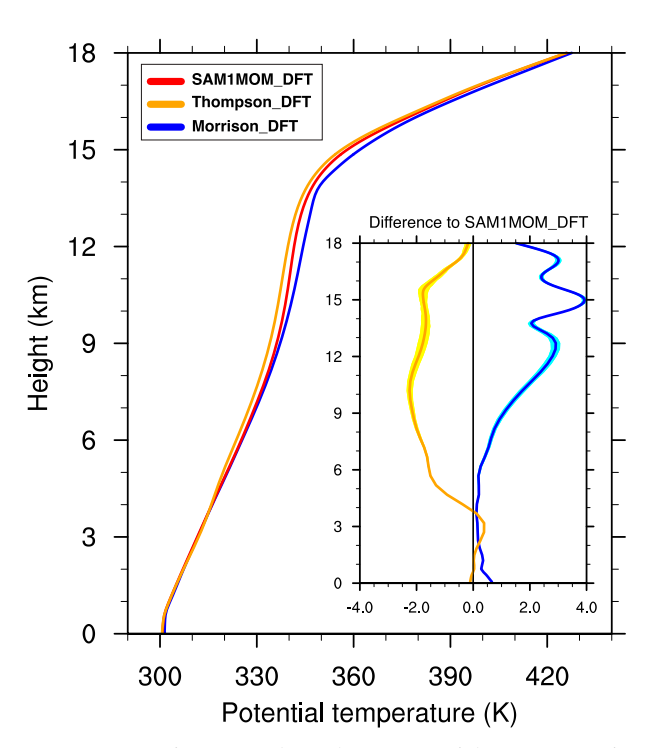


FIG. 2. Domain-averaged profiles of potential temperature in the DEFAULT set of simulations: SAM1MOM_DFT (red), Thompson_DFT (orange), and Morrison_DFT (blue). The deviation of potential temperature profile from SAM1MOM_DFT in Thompson_DFT and Morrison_DFT is shown in the embedded figure. For all the lines shown, the shading indicates the 95% confidence interval. Some portions of the uncertainty range are too small to see the shading.

section, we explore what processes contribute to the difference between the two scenarios.

4. Influence of upper-troposphere stratification and atmospheric cloud radiative effects

Why does the Morrison_DFT simulation have much weaker convective overshoots? As shown in Fig. 2, the Morrison_DFT simulation has a much warmer (~3 K) upper troposphere while the temperature in the lower troposphere is similar to that in the other two simulations. A natural hypothesis would be that the warmer and more stable upper troposphere in the Morrison_DFT simulation lowers the LNB and reduces the buoyancy, leading to much smaller updraft velocity associated with convective overshoots near the TTL.

To test this hypothesis, we performed two additional switch-profile simulations (Table 1). In the first simulation, by adding tuned and time-invariant forcing of temperature and moisture tendencies, we force the model using the Morrison scheme to maintain a temperature and moisture profile similar to the SAM1MOM_DFT simulation ("Morrison_SAMprl" herein). Similarly, in the second simulation, we force the model using the SAM one-moment scheme to maintain a temperature and moisture profile similar to the Morrison_DFT simulation ("SAM1MOM_MORprl" herein). The time-invariant

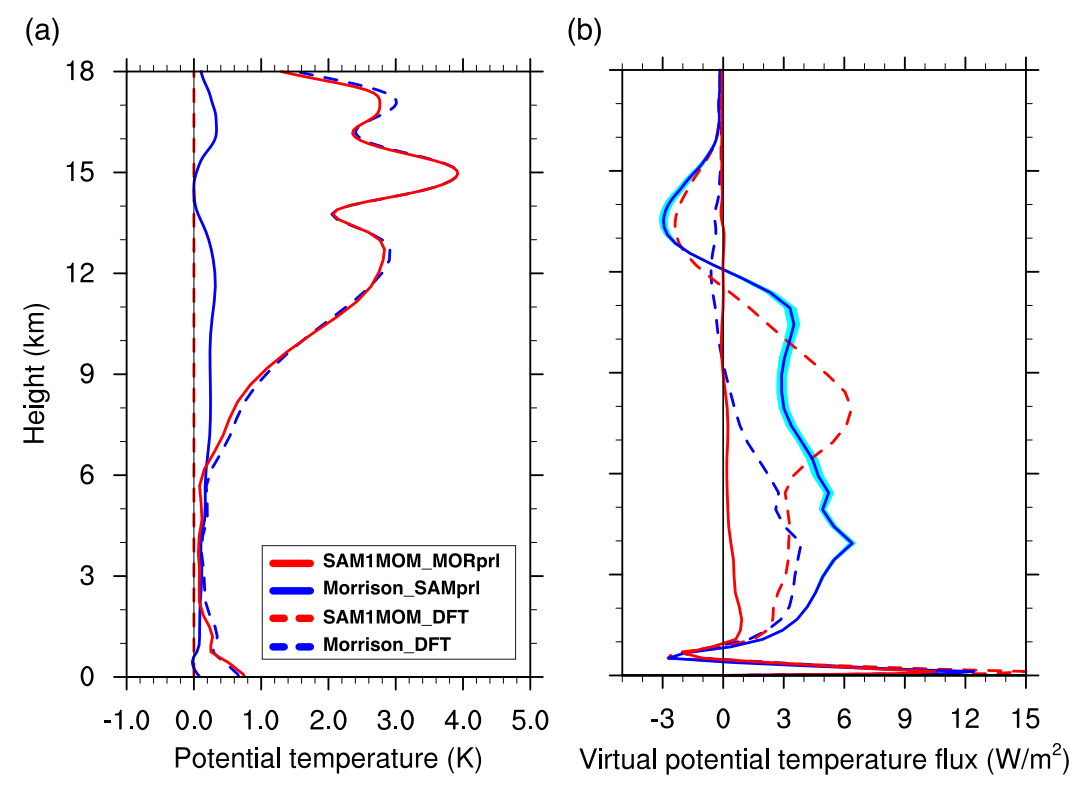


FIG. 3. (a) Domain-mean profiles of potential temperature, as the deviation from that in SAM1MOM_DFT, in the switch-profile simulations (solid) and in the default set of simulations (dashed): SAM1MOM_MORprl (solid red), Morrison_SAMprl (solid blue), SAM1MOM_DFT (dashed red), and Morrison_DFT (dashed blue). (b) As in (a), but for the virtual potential temperature flux $(\rho C_p \overline{w'\theta'_v})$. For switch-profile simulations (solid lines), the shading indicates the 95% confidence interval. Some portions of the uncertainty range are too small to see the shading.

temperature and moisture tendencies are obtained by iteratively running simulations in which we both added time-invariant tendencies (which are zero in the first iteration) and nudged the domain-averaged temperature and moisture profiles to the target profiles. The nudging time scale is 10 h. In each iteration, we ran 50 days, saved the nudging temperature and moisture tendencies (averaged over the last 20 days), and added them into the time-invariant tendencies. After four iterations, we obtained the final time-invariant tendencies and ran the two switch-profile simulations without nudging temperature and moisture. The potential temperature profiles in the switch-profile simulations shown in Fig. 3a are very close to the target profiles derived from the DEFAULT simulations.

These two new simulations clearly support that perturbation of upper-troposphere temperature profile can impact the virtual potential temperature flux and the LNB (Fig. 3b). With a colder upper troposphere than the Morrison_DFT simulation, the Morrison_SAMprl simulation now has an LNB that is slightly higher than that in the SAM1MOM_DFT simulation. The inferred convective cooling in the TTL in the Morrison_SAMprl simulation is slightly stronger but on the same order of magnitude as in the SAM1MOM_DFT simulation. The SAM1MOM_MORprl simulation indicates a much lower LNB that is closer to that in the Morrison_DFT simulation. There is no indication of downward virtual potential temperature

flux above LNB, suggesting strong suppression of deep convection and convective overshoots in the SAM1MOM_MORprI simulation. Similar switch-profile simulations are performed between the SAM1MOM and Thompson schemes and obtain similar results. The SAM1MOM_THOMprI simulation has strongly enhanced convective overshoots, while the Thompson_SAMprI simulation has strongly suppressed deep convection and convective overshoots (not shown, abbreviations follow the same rule as SAM1MOM_MORprI and Morrison_SAMprI). The switch-profile simulations suggest that the perturbation of the upper-troposphere stratification can strongly modulate the convective overshoots and LNB.

The above switch-profile results should not be interpreted as that environmental profile can uniquely determines LNB and other convective properties. The SAM1MOM_DFT and Thompson_DFT simulations have a temperature difference of about 2 K in the upper troposphere but with similar overshooting properties. The buoyancy of convective updrafts depends not only on the environmental virtual temperature but also on factors such as condensate loading in the updrafts, which decreases buoyancy and the entrainment history of the updrafts. These factors can be very different for simulations using different microphysics schemes. One should also be cautious in interpreting convective properties as a consequence of environmental profiles, because environmental

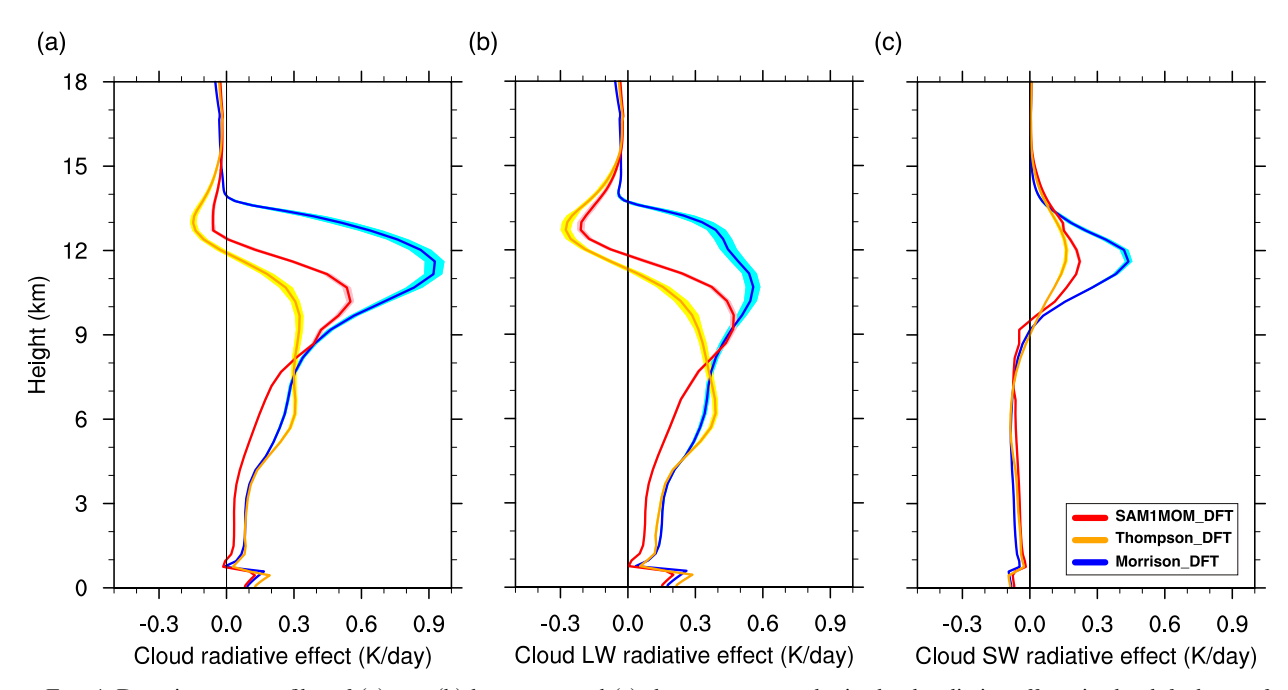


FIG. 4. Domain-mean profiles of (a) net, (b) longwave, and (c) shortwave atmospheric cloud radiative effects in the default set of simulations: SAM1MOM_DFT (red), Thompson_DFT (orange), and Morrison_DFT (blue). The shading indicates the 95% confidence interval.

profiles and convection mutually interacts with each other and are closely coupled. The mechanism we would like to explore is that processes not directly related to convection, such as large-scale circulation or radiative effect from clouds or tracer gas, can influence the upper-troposphere temperature, which can then modify the convective overshoots.

Because the only difference in the experimental setting of the three default simulations is the cloud microphysics scheme, next we explore whether the different ACRE lead to different environmental temperature profiles. The ACRE in the Morrison_DFT simulation are indeed larger in the upper troposphere than in the other two DEFAULT simulations (Fig. 4a). Both the longwave and shortwave cloud radiative effects contribute to this difference (Figs. 4b,c). The SAM1MOM_DFT and Thompson_DFT simulations have a strong longwave cloud cooling at ~13 km while the Morrison_DFT simulation fails to produce such a cooling structure. The shortwave cloud radiative heating at ~12 km in the Morrison_DFT simulation is much stronger than those in the other two simulations.

To provide causal evidence that differences in ACRE lead to different upper-troposphere stratification and different convective overshooting velocities, we ran a new set of three simulations with the three microphysics schemes with the cloud radiative effects turned off. We call this set of simulations the NOCRE set (Table 1), in contrast with the DEFAULT set, and we refer to individual NOCRE simulations as SAM1MOM_NOCRE, Thompson_NOCRE, and Morrison_NOCRE. In the NOCRE simulations, the radiation model ignores the presence of any cloud condensate (both precipitating and nonprecipitating) and returns the clear-sky radiation. After turning off the cloud radiative

effect, the Morrison_NOCRE simulation experiences the largest temperature decrease and becomes even colder in most of the troposphere compared to the SAM1MOM_NOCRE simulation (Figs. 5a,b). The Morrison scheme still produces warmer TTL than the SAM1MOM scheme, which is likely related to the radiative effect of different water vapor mixing ratio in the TTL (Fig. 5c).

The properties of the convective overshoots in the NOCRE simulations are illustrated in Fig. 6. After turning off the cloud radiative effect, the Morrison_NOCRE simulation shows a significantly stronger convective cooling in the TTL (~-0.15 K day⁻¹), although the convective cooling in the TTL is still somewhat weaker than the SAM1MOM_NOCRE simulation and the Thompson_NOCRE simulation (Fig. 6a). The LNB in the Morrison_NOCRE simulation converges to those in the other two simulations (Fig. 6b). Also, the shift from the DEFAULT set to the NOCRE set in the Morrison simulation indicates a significant increase in the frequency of occurrence of strong updraft (Fig. 6c). Therefore, the NOCRE simulations provide evidence of the causal effect between the stronger ACRE and the weaker convective overshoots in the default Morrison simulation.

One may notice that, in the SAM1MOM_NOCRE and Thompson_NOCRE simulations, the LNB is in fact slightly lower than in their DEFAULT counterpart (comparing Fig. 1b and Fig. 6b). The Thompson_NOCRE simulation also produces lower occurrence of strong updraft than the Thompson_DFT simulation (Fig. 6c). The different behavior to the Morrison scheme is related to the water vapor change in the lower troposphere in the NOCRE runs (Fig. 5d). If the temperature profile remains unchanged and only the lower troposphere

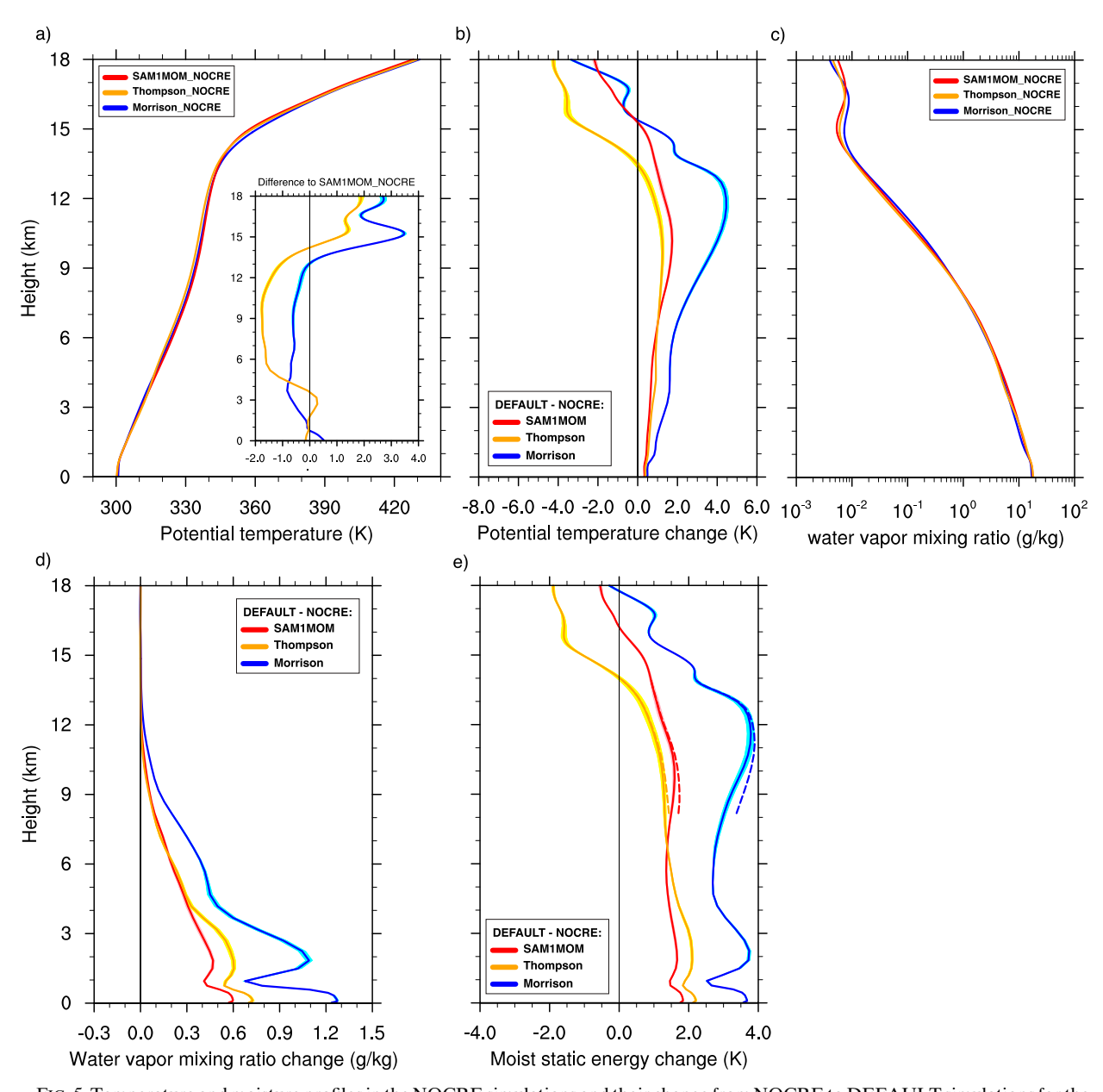


FIG. 5. Temperature and moisture profiles in the NOCRE simulations and their change from NOCRE to DEFAULT simulations for the three microphysics schemes. (a) As in Fig. 2, but for the NOCRE set of simulations. (b) The potential temperature changes from NOCRE to DEFAULT simulations. (c) The profiles of water vapor mixing ratio for the NOCRE simulations. (d) The change of water vapor mixing ratio from NOCRE to DEFAULT simulations. (e) The change of moist static energy (solid lines) and the change of saturation moist static energy (dashed lines, only the values in the upper troposphere between 8 and 14 km are shown) from NOCRE to DEFAULT simulations. The shading indicates the 95% confidence interval.

becomes drier, the convective updraft will become less buoyant and the LNB will become lower. The combined effect of changes in temperature and moisture can be seen in the change of the moist static energy (MSE; shown as MSE/C_p in Fig. 5e with the unit of K), which is roughly conserved in moist adiabatic processes. To connect MSE change with the change of LNB, let us consider the buoyancy change of a saturated convective updraft plume at a fixed height, for example, the LNB in the DEFAULT run. The buoyancy is proportional to

the virtual temperature of the plume minus the virtual temperature of the environment. The temperature difference at a given pressure level can be indicated by the saturation MSE difference. The saturation MSE change in the saturated updraft plume equals to the mixture of MSE change at a range of lower levels where the rising plume originates and where the unsaturated environmental air was entrained into the rising plume. The saturation MSE change in the environment in the upper troposphere (Fig. 5e dashed lines) is very close to MSE

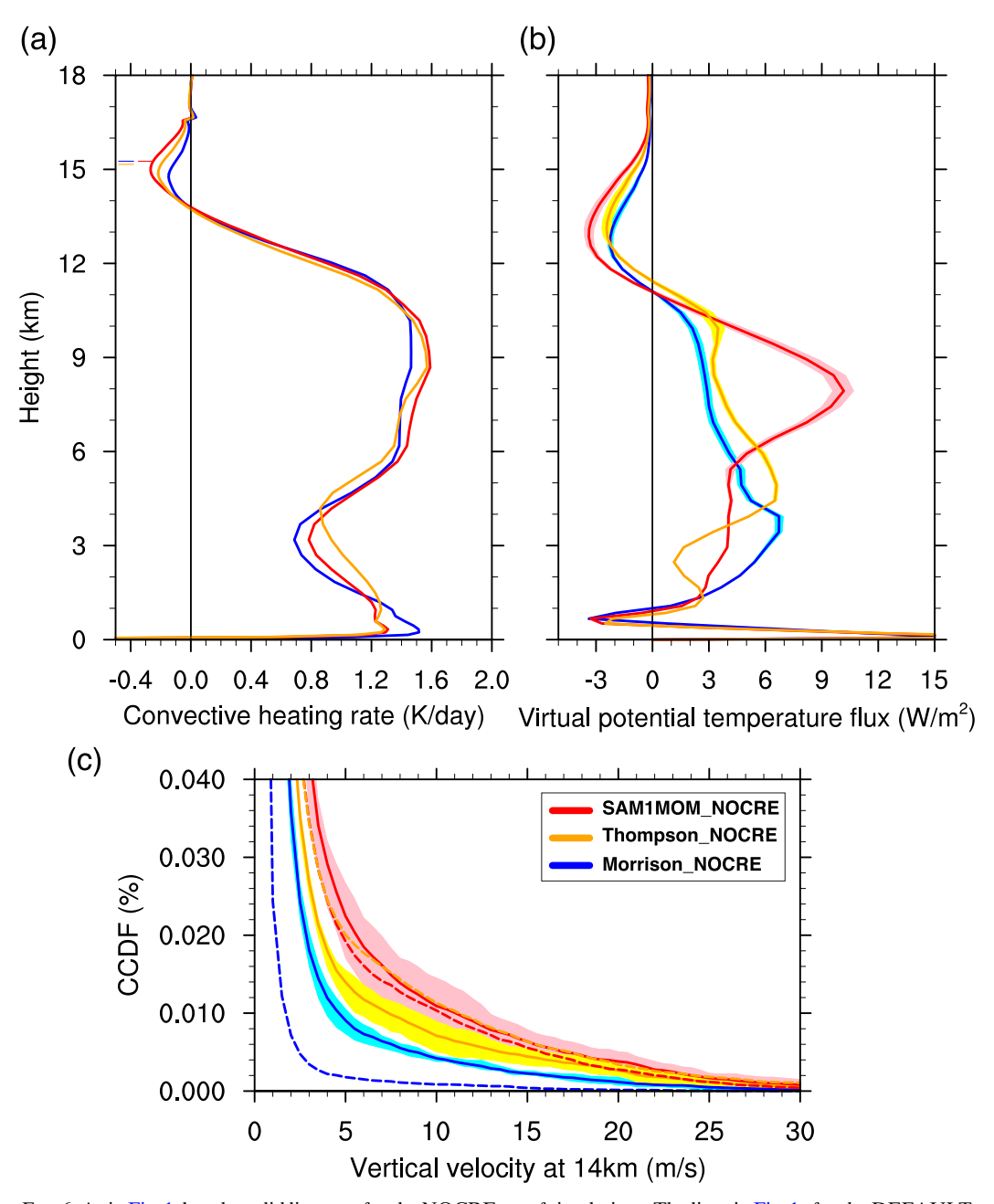


FIG. 6. As in Fig. 1, but the solid lines are for the NOCRE set of simulations. The lines in Fig. 1c for the DEFAULT set of simulations are overlaid in (c) as dashed lines for reference.

change. For the Thompson_DFT and Thompson_NOCRE simulations (same for the SAM1MOM simulations) at 12 km, which is roughly the LNB in these runs, the saturation MSE change (DEFAULT minus NOCRE) is smaller than the MSE change below. Therefore, an updraft at 12 km tends to be less buoyant in the Thompson_NOCRE simulation than in the Thompson_DFT simulation. That is, the LNB will become lower in the Thompson_NOCRE simulation than in the Thompson_DFT simulation. On the contrary, for the Morrison simulations, the cloud radiative heating is so strong in the

upper troposphere that the saturation MSE change at 9–12 km is larger than MSE change at 4–9 km. Therefore, the LNB becomes higher in the Morrison_NOCRE simulation than in the Morrison_DFT simulation.

To investigate the separate impact of longwave and shortwave cloud radiative effect, we perform two additional simulations using Morrison scheme in which we turn off only longwave or shortwave ACRE (Morrison_NOCRELW and Morrison_NOCRESW). Because both the longwave and shortwave ACRE have a positive peak in the upper troposphere

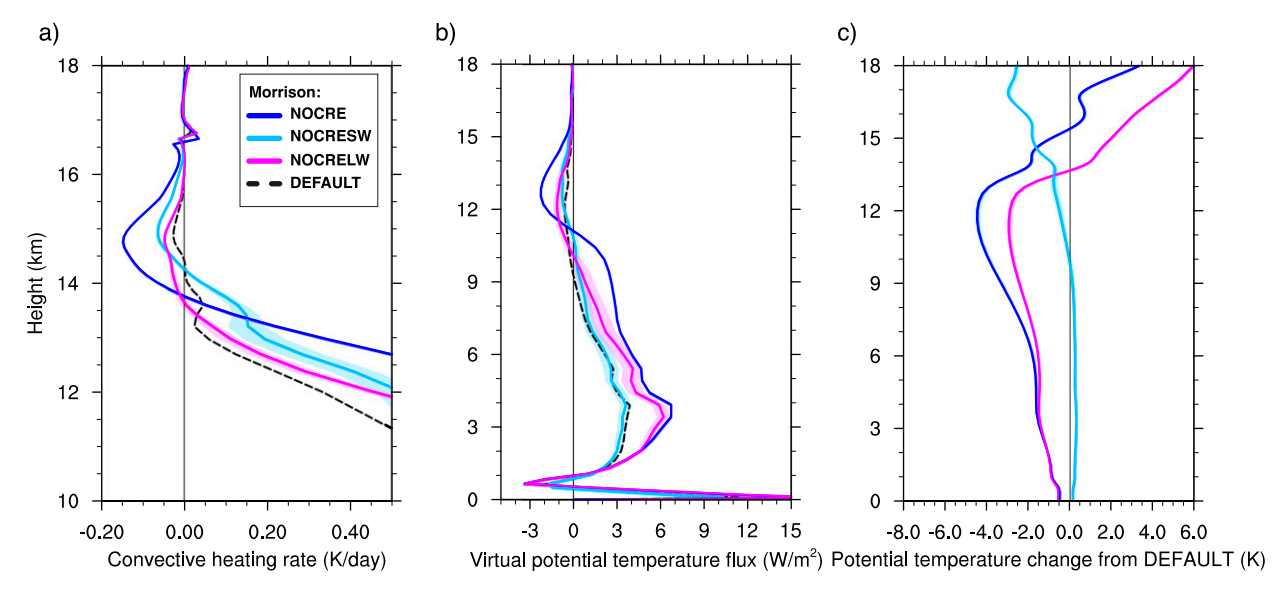


FIG. 7. (a) The convective heating rate, (b) virtual potential temperature flux, and (c) potential temperature deviation from the Morrison_DFT simulation for the Morrison_NOCRE (dark blue), Morrison_NOCRESW (light blue), Morrison_NOCRELW (magenta), and Morrison_DFT (dashed black) simulations. The shading for the NOCRESW and NOCRELW simulations indicates the 95% confidence interval.

(Figs. 4b,c), turning off either longwave or shortwave ACRE weakens the stratification between 8 and 11 km (Fig. 7c) and therefore can lead to enhanced overshooting cooling and lifted LNB (Figs. 7a,b). The overall tropospheric longwave ACRE is stronger than the shortwave ACRE, which is mainly concentrated in the upper troposphere. Therefore, the Morrison_ NOCRELW simulation has stronger upper and overall troposphere cooling than the Morrison_NOCRESW simulation and has smaller buoyancy frequency (not shown) between 6 and 10 km. However, the lower troposphere drying, which by itself can weaken convective updrafts, in the Morrison_NOCRE simulation (Fig. 5d) almost all comes from turning off the longwave ACRE. After combining the effect of both stratification and water vapor change, the Morrison_NOCRELW and Morrison_NOCRESW simulations produce a comparable enhancement of convective cooling in the TTL.

5. Understanding the different ACRE associated with different microphysics schemes

To understand the ACRE difference in the upper troposphere across the DEFAULT simulations, we show in Fig. 8a the probability distribution of vertically integrated optical depth of the sum of radiatively active and frozen hydrometeors. For all the frozen hydrometeors, only cloud ice is radiatively active in the SAM one-moment scheme, while both the cloud ice and snow are radiatively active in the Morrison and Thompson schemes. The optical depth is for the 625–778-nm band. For a longwave band near $10.5\,\mu\text{m}$, the optical depth distribution shown in Fig. 8a slightly shifts to smaller optical depths but retains the shape (not shown). The cloud optical depth distribution can be largely explained by the distribution of vertically integrated ice (plus snow for the Morrison and Thompson simulations) water path (Fig. 8b). For simplicity, we

will use RFWP to refer to the radiatively active frozen water path for all three schemes. The Morrison_DFT simulation shows a clear distinction from the other two simulations, with much higher frequency of occurrence for clouds with optical depths in the range of 0.01-1, roughly corresponding to RFWP in the range of $10^{-4}-10^{-2}$ kg m⁻². Figure 8c also shows that the Morrison_DFT simulation has a larger cloud fraction than the other two simulations in the upper troposphere.

To further relate the distribution of RFWP to the domainmean vertical distribution of ACRE, we show in Fig. 9 the vertical distribution of ACRE, cloud ice and snow content and effective radius sorted by different RFWP bins. That is, we sort all the columns according to their RFWP and average over the columns in the same bins. The ACRE sorted by RFWP shares some common feature across the three schemes. For RFWP greater than $10^{-1} \,\mathrm{kg}\,\mathrm{m}^{-2}$, which corresponds to convective cores, there is strong cloud-top cooling in the upper troposphere. For smaller RFWP corresponding to anvil clouds or thin cirrus, there is generally cloud radiative heating in the upper troposphere. Therefore, the much larger occurrence of RFWP between 10^{-4} and 10^{-2} kg m⁻² for the Morrison_DFT simulation could indeed contribute to the larger total ACRE in the upper troposphere. The Thompson_DFT simulation has a higher occurrence of RFWP above $10^{-1}\,\mathrm{kg}\,\mathrm{m}^{-2}$, which contributes to the stronger cloud cooling above 12km in the Thompson_DFT simulation than the other two simulations. The Thompson_DFT simulation also produces a large amount of very thin clouds with RFWP less than $10^{-6} \,\mathrm{kg}\,\mathrm{m}^{-2}$, but these clouds are too optically thin and contributes little to the ACRE.

In addition to cloud cover, the difference in vertical distribution of cloud condensate and effective radius could also contribute to the ACRE difference. For RFWP between 10^{-4} and 10^{-2} kg m⁻², the ACRE in the upper troposphere in the Morrison_DFT simulation is similar to that of the

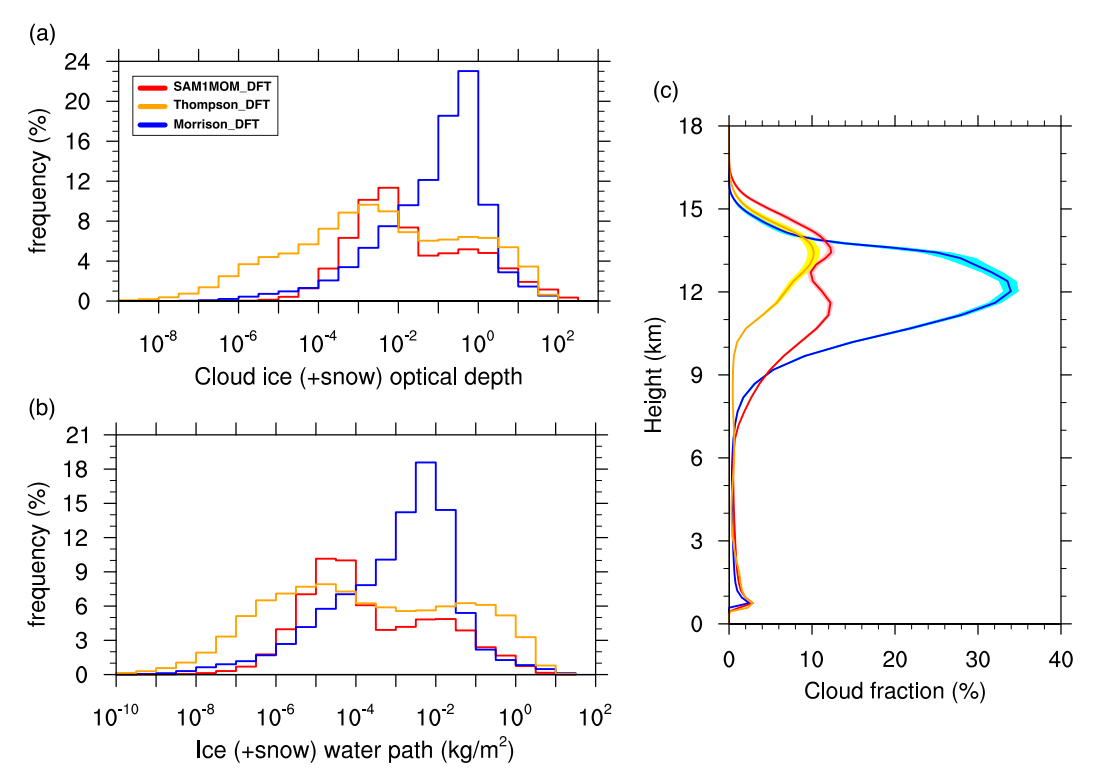


FIG. 8. The relative frequency histograms of (a) the vertically integrated optical depth and (b) water path for the sum of radiatively active frozen hydrometeors in the default set of simulations: SAM1MOM_DFT (red), Thompson_DFT (orange), and Morrison_DFT (blue). The optical depth is for the 625–778-nm band. In the Morrison and Thompson simulations, both cloud ice and snow are radiatively active, while in the SAM1MOM simulation only cloud ice is radiatively active. The frequency is normalized by the number of total sampled grids including both clear-sky and cloudy-sky grid points. (c) The cloud fraction profiles with shading indicating 95% confidence interval.

SAM1MOM_DFT simulation and is much stronger than that of the Thompson_DFT simulation (note that the color bar is not linear). This is related to the difference in the vertical distribution of frozen mass and effective radius. The frozen mass is mostly cloud ice for the Morrison_DFT and SAM1MOM_ DFT simulations (Figs. 9d,e,g) but is primarily snow for the Thompson_DFT simulation (Figs. 9f,h). The vertical distribution of cloud ice in the Morrison_DFT and SAM1MOM_DFT simulations is also located at higher levels but with a narrower range of height than the vertical distribution of snow in the Thompson_DFT simulation, which could explain the sharper vertical gradient of ACRE in the midtroposphere in the Morrison DFT and SAM1MOM DFT simulations (Fig. 4a). The effective radius for the majority of snow in the Thompson_ DFT simulation is greater than 150 μ m, while the effective radius for the majority of the cloud ice in the other two simulations is below 50 µm (Figs. 9i,j,k). Therefore, the same amount of radiatively active frozen mass will have smaller total cross section and thus smaller optical depth in the Thompson scheme.

6. Discussion

a. Sensitivity to model resolution

The above simulations use horizontal resolution of 1 km. However, turbulence below 1-km scale may have a significant

impact on processes like irreversible mixing of convective overshoots, convective entrainment, or the behavior of microphysics schemes. To better resolve these processes, we increase the horizontal resolution to $100\,\mathrm{m}$ for the SAM1MOM and Morrison simulations (herein SAM1MOM_100m and Morrison_100 m, Table 1). The domain size is reduced to $32\,\mathrm{km}\times32\,\mathrm{km}$ to optimize the computational cost. A 20-day period after spinup is used for the analysis. Other than the horizontal domain size and the horizontal resolution, all settings are identical to those of the DEFAULT simulations.

The dependence of convective overshoots on microphysics scheme in 100-m-resolution simulations is consistent with the DEFAULT simulations. Compared with the SAM1MOM_100m simulation, the Morrison_100m simulation still produces a much weaker overshooting cooling, weaker downward heat flux, and lower LNB (Figs. 10a,b). Within the TTL, the difference in heating rate and heat flux between 100-m- and 1-km-resolution runs is much smaller than the difference between two microphysics schemes.

It is interesting to notice that in the 100-m-resolution simulations, the cloud fraction in the upper troposphere is significantly larger than in the 1-km-resolution simulations (Fig. 10c). The maximum cloud fraction in the upper troposphere increases from 12% in the DEFAULT simulation to 21% in the 100-m-resolution simulation for SAM1MOM scheme, and

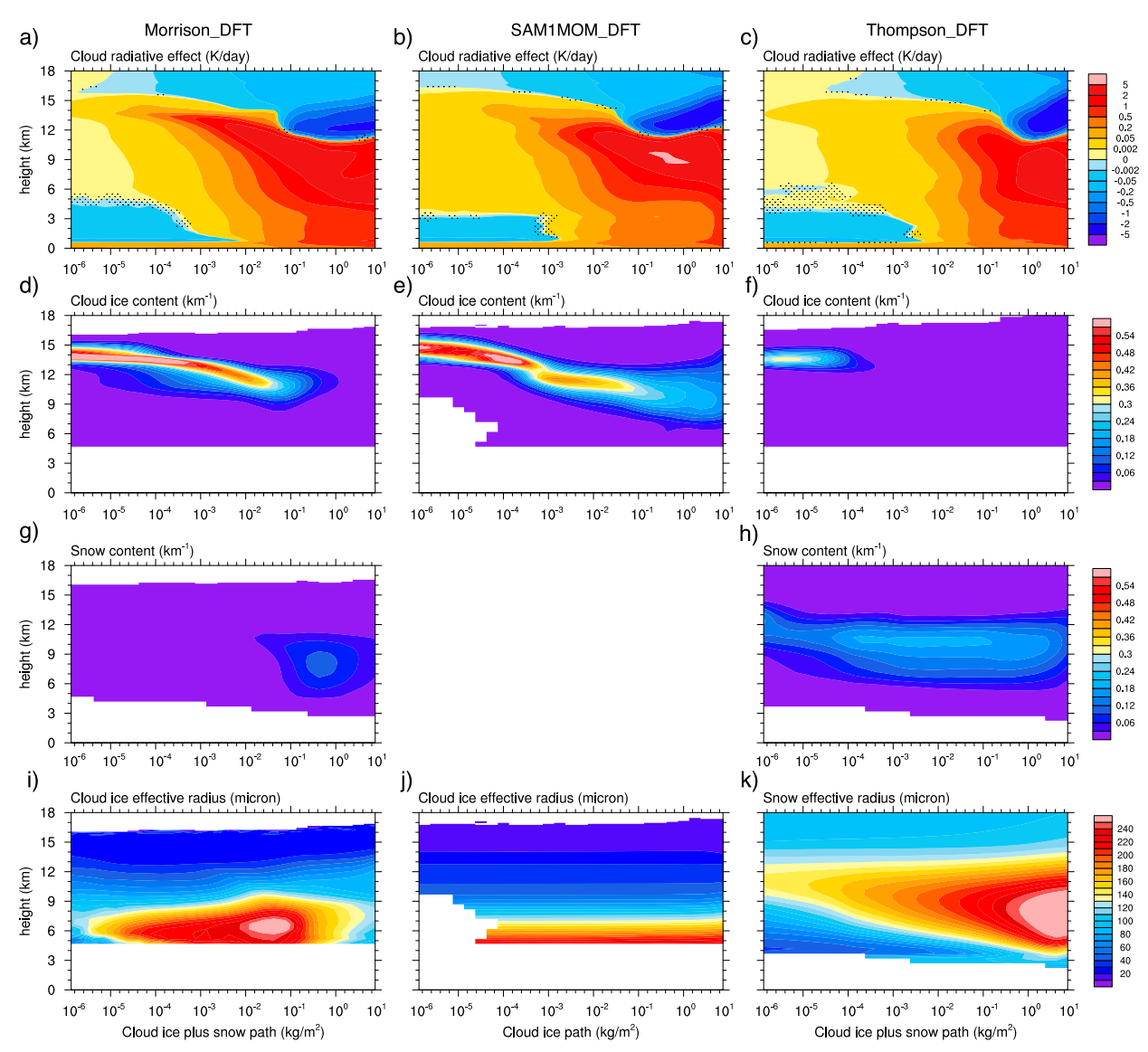


FIG. 9. Vertical distribution of (a)–(c) cloud radiative effect, (d)–(f) cloud ice content, (g),(h) snow content, and (i)–(k) frozen hydrometer effective radius sorted by model columns with different values of frozen water path. (left) Morrison_DFT. (center) SAM1MOM_DFT. The snow content in the SAM1MOM simulations is not radiatively active so we do not show the snow content here for SAM1MOM_DFT. (right) Thompson_DFT. The cloud ice content and snow content (g m $^{-3}$) is normalized by the total frozen water path (g m $^{-2}$) is each bin, so the unit becomes km $^{-1}$. The normalized cloud ice/snow contents also represent the vertical probability distribution of frozen mass in each bin. In (i)–(k), we show the cloud ice effective radius for Morrison_DFT and SAM1MOM_DFT but snow effective radius for Thompson_DFT, because cloud radiative effective is dominated by cloud ice in the SAM1MOM and Morrison simulations but is dominated by snow in the Thompson simulations.

from 34% to 49% for the Morrison scheme. The higher cloud fraction leads to stronger cloud radiative heating in the upper troposphere, which explains the weaker convective heating in the upper troposphere in Fig. 10a. To make an apples-to-apples comparison, the 100-m-resolution output fields (e.g., 3D temperature, cloud water and cloud ice mixing ratio) are regridded to match the coarser 1-km grid, by averaging fine-grid fields in $1 \text{ km} \times 1 \text{ km}$ chunks. The cloud fraction based on regridded output is even larger than the cloud fraction based on the raw 100-m-resolution output fields (Fig. 10c). This result suggests a

significant enhancement of cloud fraction by resolved processes at the 100-m scale, although further study is needed to narrow down the exact mechanisms.

b. Implication for TTL heat balance and cold-point tropopause

Our results have implications for the debate, as we mentioned in the introduction, of whether the observed radiative heating in the TTL is mainly balanced by convective cooling or by adiabatic cooling due to eddy-driven circulation.

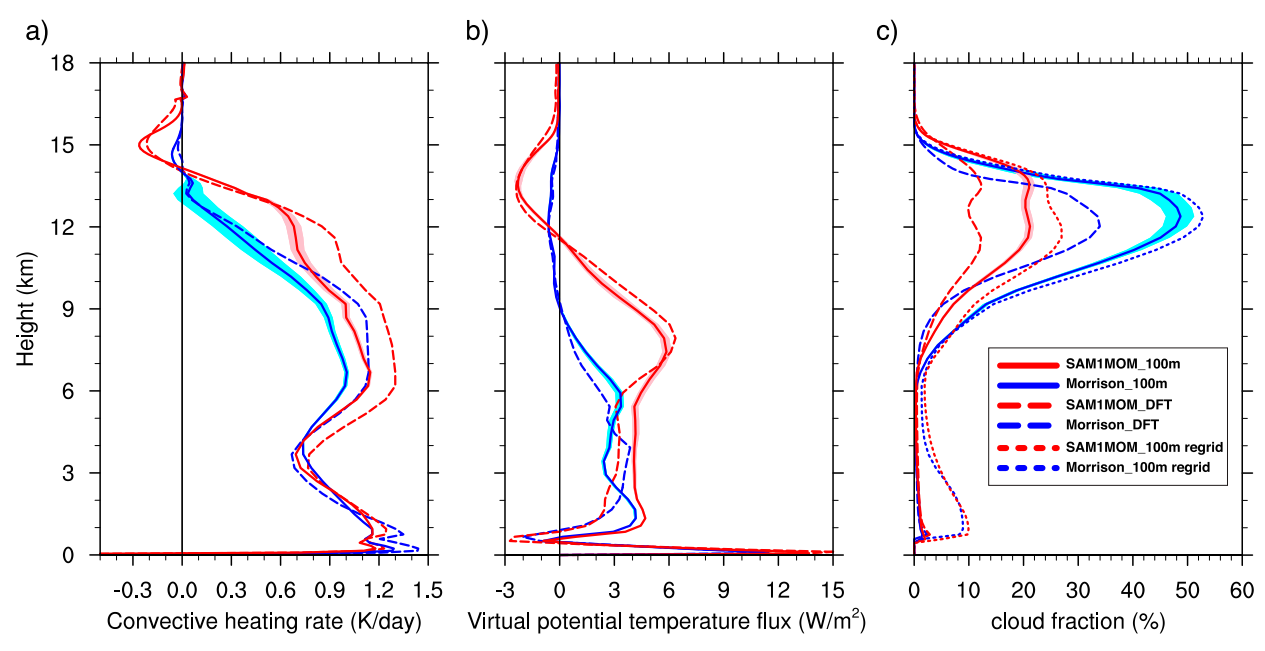


FIG. 10. (a) The convective heating rate, (b) virtual potential temperature flux, and (c) cloud fraction for the SAM1MOM_100m (solid red lines) and Morrison_100m (solid blue lines). The SAM1MOM_DFT and Morrison_DFT are represented as long-dashed lines for reference. The short-dashed lines in (c) represent the cloud fraction after regridding the 100-m-resolution simulations from 100-m resolution to 1-km resolution.

We perform a set of simulations in which we impose a fixed large-scale vertical velocity mimicking the upwelling of Brewer-Dobson circulation (Fig. 11a). This set of simulations is called the BDC set, and the individual simulations are SAM1MOM_ BDC, Thompson_BDC, and Morrison_BDC (Table 1). In the BDC simulations, the three microphysics schemes continue to produce the hard-landing and soft-landing scenarios. Similar to the Morrison_DFT simulation, the Morrison_BDC simulation still produces a soft-landing scenario, with a much lower LNB and weaker downward heat flux associated with convective overshoots (Fig. 11b) than the other two schemes. The imposed upwelling makes the atmosphere significantly colder above 13 km than the DEFAULT simulations but has little impact on temperature below 13 km (Fig. 11c). Furthermore, the imposed upwelling has a very limited impact on the strength of downward heat flux associated with overshoots (comparing Fig. 11b with Fig. 1b). For the heat balance in the TTL, in the soft-landing scenario, the radiative heating is dominantly balanced by the adiabatic heating from large-scale forcing representing the eddydriven ascent, with little contribution from deep convection (Fig. 11d). In the hard-landing scenario, convective cooling and large-scale forcing make comparable contributions to balance the radiative heating (Figs. 11e,f).

Another relevant debate is whether the height of the coldpoint tropopause (CPT) is coupled to deep convection (e.g., Thuburn and Craig 2002; Kuang and Bretherton 2004; Fueglistaler et al. 2009; Fu et al. 2018). In the hard-landing scenario (the DEFAULT and NOCRE simulations with the single-moment scheme and the Thompson scheme and without any large-scale forcing), the cold-point tropopause is collocated with the height of the strongest convective cooling (red and orange horizontal lines in Figs. 1a and 6a), which is consistent with Kuang and Bretherton (2004). It is reasonable to imagine that a small change in the height of the strongest convective cooling could directly influence the CPT by changing the shape of the temperature profile. With the large-scale upwelling, the cold-point tropopause is shifted higher and somewhat decoupled from the height of the strongest convective cooling (Figs. 11e,f). In the soft-landing scenario, the cold-point tropopause shows a clear separation from deep convection (Fig. 11d and blue horizontal lines in Figs. 1a and 6a). In this case, a small and smooth change in the convective cooling profile should not directly affect the CPT.

c. Potential impact from varying ozone concentration to convective overshoots

In this section we explore whether the variation of ozone concentration could impact the strength of convective overshoots. The seasonal cycle of ozone can lead to significant temperature variations near and above the tropopause (e.g., Fueglistaler et al. 2011). Therefore, one may wonder whether ozone has the potential to impact the strength of convective overshoots through modifying the stratification below the TTL.

To get the seasonal cycle of ozone concentration in the tropics, we use monthly ozone concentration from ERA5 data (Hersbach et al. 2020) and average them within 30°S–30°N over the period of 2010–19. We choose two ozone profiles for February and August to represent the largest ozone variation in the TTL. These two profiles, in addition to the ozone profile used in the DEFAULT simulations, are shown in Fig. 12a. Then, we perform a set of ozone simulations (Table 1), in which

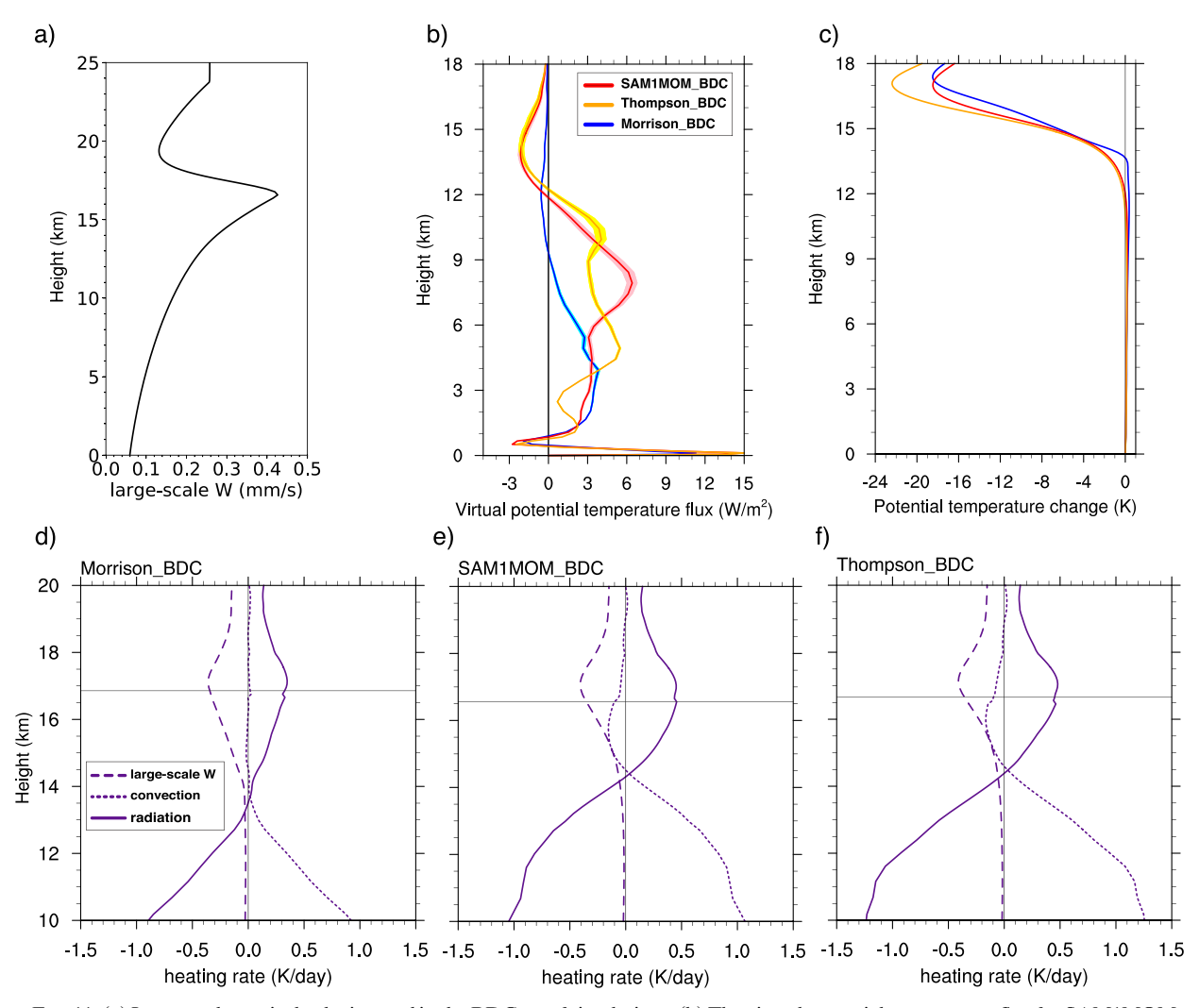


FIG. 11. (a) Large-scale vertical velocity used in the BDC set of simulations. (b) The virtual potential temperature flux for SAM1MOM_BDC (red), Thompson_BDC (orange), and Morrison_BDC (blue). (c) Potential temperature change from the DEFAULT set to the BDC set of simulations. (d) The heat balance in the Morrison_BDC simulation. The solid purple line is the radiative heating rate. The dashed purple line is the adiabatic heating rate due to large-scale vertical velocity. The dotted purple line is the convective heating rate. The horizontal black line indicates the cold-point tropopause. (e) As in (d), but for SAM1MOM_BDC. (f) As in (d), but for Thompson_BDC.

we use SAM one-moment scheme with the February and August ozone profiles (SAM1MOM_Feb and SAM1MOM_Aug).

Figure 12b shows that the change in temperature due to the ozone seasonal cycle is very small below $12\,\mathrm{km}$ (<0.3 K), although there is a large temperature variation in the TTL. This small temperature difference near the LNB is not large enough to significantly impact convective overshoots. As shown in Fig. 12c, the profiles of virtual potential temperature flux of the SAM1MOM_DFT, SAM1MOM_Feb, and SAM1MOM_Aug simulations almost overlap on each other. To get a temperature difference comparable to the temperature difference between the SAM1MOM_DFT and Morrison_DFT, we try to uniformly increase the ozone concentration in the upper troposphere between 10 and 14 km. The orange line in Fig. 12a shows an increase of ozone concentration of $2\,\mathrm{mg\,kg^{-1}}$ (1207 ppmv), which warms the upper troposphere by $\sim 1\,\mathrm{K}$ (Fig. 12b) and

weakens the maximum downward virtual potential temperature flux from 2.5 to $1.6 \,\mathrm{W \, m^{-2}}$ (Fig. 12c).

Our limited simulations suggest that, under the current RCE framework and SST of 30.5°C, the seasonal cycle of tropical ozone concentration may not have a significant impact on convective overshoots. To warm the upper troposphere by a comparable amount to the cloud radiative effect, we need to increase the ozone concentration in the upper troposphere to an unrealistic high value. However, our results do not exclude the possibility for ozone (and similarly eddy-driven upwelling mentioned in the previous section) to influence convective overshoots. Even though the SST we used is similar to that of the western Pacific warm pool, the LNB in the RCE simulations may not represent a realistic situation. Including large-scale Hadley-like or Walker-like circulation might lift the LNB to higher levels. If the LNB can be lifted by including

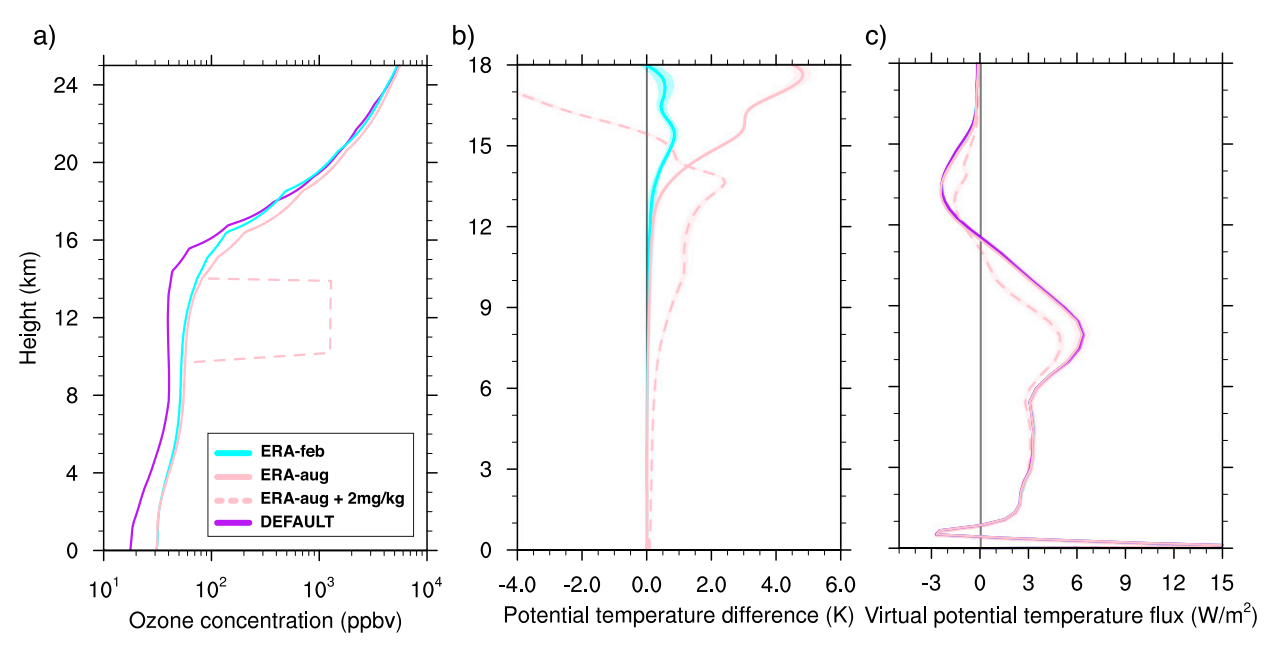


FIG. 12. (a) Profiles of ozone concentration used in this study, (b) potential temperature deviation from SAM1MOM_DFT, and (c) virtual potential temperature flux for SAM1MOM_FEB (cyan), SAM1MOM_Aug (solid pink), SAM1MOM_Aug+2 (dashed pink), and SAM1MOM_DFT (purple).

large-scale circulation to a level where the ozone variation and eddy-driven upwelling can drive significant temperature change (e.g., on the order of 1 K), the variation in ozone concentration and eddy-driven upwelling could then easily modify the strength of convective overshoots. It is also unknown whether in a warmer climate, as troposphere gets deeper, the LNB becomes higher and could be more easily influenced by the variation of ozone or eddy-driven upwelling. Future study is needed to explore these possibilities.

7. Summary

In this study, we sought to study what processes can influence the strength of cooling in the TTL by convective overshoots. We carried out RCE simulations with a threedimensional cloud-resolving model SAM. To this aim, we explored three distinct microphysics schemes. We found that the choice of cloud-microphysics scheme can substantially influence the strength of convective cooling in the TTL through modifying the upper-troposphere stratification. Two of the microphysics schemes (SAM single-moment scheme and Thompson double-moment scheme) produce a hard-landing scenario: frequent occurrence of convective overshoots reaching the TTL with strong updrafts, high LNB (~12 km), and a substantial convective cooling in the TTL (with a minimum heating rate of $\sim -0.2 \,\mathrm{K}\,\mathrm{day}^{-1}$). On the other hand, the other double-moment scheme (Morrison scheme) produces a soft-landing scenario: rare occurrence of strong convective overshoots reaching the TTL, low LNB $(\sim 9.5 \,\mathrm{km})$, and a much weaker convective cooling in the TTL (with a minimum heating rate of $\sim -0.03 \,\mathrm{K} \,\mathrm{day}^{-1}$). The difference between the hard-landing and soft-landing scenarios largely results from the difference in the uppertroposphere stratification, which is related to different cloud-radiation interaction across schemes. The stronger ACRE produced by the Morrison scheme generates a warmer and more stable upper troposphere, which acts as a buffer zone below the TTL and consequently slows down the convective updrafts and lowers the LNB. This stratification mechanism also suggests the possibility for ozone variation or eddy-driven upwelling in the TTL to modulate the strength of convective overshoots. We further test the sensitivity of overshooting cooling to changes in model resolution by increasing the horizontal resolution to 100 m. The corresponding change of overshooting cooling is much smaller compared with the difference between the hardlanding and soft-landing scenarios. These results highlight the importance of cloud microphysics and ACRE to accurately simulate the convective influence on the TTL. Also, this study suggests that the treatment of cloud microphysics may be one of the reasons for the disagreement on the importance of convective cooling in the TTL by previous numerical studies (Kuang and Bretherton 2004; Küpper et al. 2004; Robinson and Sherwood 2006). Although this study only focuses on the heat budget, the difference in the strength of convective overshoots could also potentially have a major impact on the water budget in the TTL.

However, it is still unclear which scenario (hard-landing or soft-landing) and which cloud-microphysics scheme is more realistic when compared to the observations. Tropical ACRE show large discrepancies between observation, reanalysis, and climate models (Voigt et al. 2019; Fu et al. 2018). Even in our RCE simulations, increasing the horizontal resolution from 1 km to 100 m can significantly increase cloud fraction and

ACRE. In reality, ACRE also have large spatial contrast between large-scale subsidence region and convective region. It is therefore hard to simply compare ACRE in RCE simulations to observation to infer which microphysics scheme produces more realistic scenario on convective overshoots. For the study of convective overshoots in the TTL, one possible way to reduce the uncertainty from ACRE can be to nudge the domain mean cloud radiative heating rate toward ACRE estimated from observational cloud fields (e.g., Fu et al. 2018) in the RCE and more complicated experiment setups. To do this, one should be careful about the uncertainties in cloud observations and possible mismatches of the vertical cloud height between observation and simulations due to surface conditions or other experimental setup details.

One limitation of this study is the idealized experimental settings (e.g., small-domain radiative-convective equilibrium simulation, no large-scale circulation, no horizontal wind shear, fixed ozone profile). Many interesting questions can be explored with a systematic increase in the complexity of the experimental setup. What is the impact of including large-scale tropospheric circulation on the height of LNB and convective overshoots? What is the relative role of deep convection and eddy-driven circulation in TTL heat budget in a near-global or a long tropical-channel cloud-resolving simulation? Could seasonal cycle of ozone concentration and eddy-driven upwelling in the TTL significantly modify the temperature near the LNB in more realistic simulations? Further research to address these questions can potentially improve the current understanding of the role of deep convection in the heat balance in the TTL and may help predict the responses of TTL in a changing climate.

Acknowledgments. We thank Marat Khairoutdinov for making the SAM model available; Peter Blossey and Blaž Gasparini for sharing their version of SAM source code; Pak Wah Chan and Xin Wei for technical help on running SAM on Cannon cluster; and Stephan Fueglistaler, Ding Ma, Nathanael Wong, and Duo Chan for fruitful discussion. Z.K., Z.H., and F.L. acknowledge the funding from NSF Grant 1743753. Z.H. acknowledges Grant DGE1745303 from NSF Graduate Research Fellowships Program.

Data availability statement. All the data used in this study are openly available at Harvard Dataverse repository at https://doi.org/10.7910/DVN/6QKJIY.

REFERENCES

- Anderson, J. G., and Coauthors, 2017: Stratospheric ozone over the United States in summer linked to observations of convection and temperature via chlorine and bromine catalysis. *Proc. Natl. Acad. Sci. USA*, **114**, E4905–E4913, https://doi.org/10.1073/pnas.1619318114.
- Bao, J. W., S. A. Michelson, and E. D. Grell, 2019: Microphysical process comparison of three microphysics parameterization schemes in the WRF Model for an idealized squall-line case study. *Mon. Wea. Rev.*, 147, 3093–3120, https://doi.org/10.1175/ MWR-D-18-0249.1.
- Bretherton, C. S., and M. F. Khairoutdinov, 2015: Convective self-aggregation feedbacks in near-global cloud-resolving

- simulations of an aquaplanet. J. Adv. Model. Earth Syst., 7, 1765–1787, https://doi.org/10.1002/2015MS000499.
- Brewer, A. W., 1949: Evidence for a world circulation provided by the measurements of helium and water vapour distribution in the stratosphere. *Quart. J. Roy. Meteor. Soc.*, **75**, 351–363, https://doi.org/10.1002/qj.49707532603.
- Butchart, N., 2014: The Brewer-Dobson circulation. *Rev. Geophys.*, **52**, 157–184, https://doi.org/10.1002/2013RG000448.
- Dacie, S., and Coauthors, 2019: A 1D RCE study of factors affecting the tropical tropopause layer and surface climate. J. Climate, 32, 6769–6782, https://doi.org/10.1175/JCLI-D-18-0778.1
- Deardorff, J. W., G. E. Willis, and B. H. Stockton, 1980: Laboratory studies of the entrainment zone of a convectively mixed layer. *J. Fluid Mech.*, **100**, 41–64, https://doi.org/ 10.1017/S0022112080001000.
- Dessler, A. E., M. R. Schoeberl, T. Wang, S. M. Davis, and K. H. Rosenlof, 2013: Stratospheric water vapor feedback. *Proc. Natl. Acad. Sci. USA*, 110, 18 087–18 091, https://doi.org/10.1073/pnas.1310344110.
- Feng, Z., L. R. Leung, R. A. Houze, S. Hagos, J. Hardin, Q. Yang, B. Han, and J. Fan, 2018: Structure and evolution of mesoscale convective systems: Sensitivity to cloud microphysics in convection-permitting simulations over the United States. *J. Adv. Model. Earth Syst.*, 10, 1470–1494, https://doi.org/10.1029/2018MS001305.
- Fu, Q., M. Smith, and Q. Yang, 2018: The impact of cloud radiative effects on the tropical tropopause layer temperatures. *Atmosphere*, **9**, 377, https://doi.org/10.3390/atmos9100377.
- Fueglistaler, S., A. E. Dessler, T. J. Dunkerton, I. Folkins, Q. Fu, and P. W. Mote, 2009: Tropical tropopause layer. Rev. Geophys., 47, RG1004, https://doi.org/10.1029/2008RG000267.
- —, P. H. Haynes, and P. M. Forster, 2011: The annual cycle in lower stratospheric temperatures revisited. *Atmos. Chem. Phys.*, **11**, 3701–3711, https://doi.org/10.5194/acp-11-3701-2011.
- Hartmann, D. L., B. Gasparini, S. E. Berry, and P. N. Blossey, 2018: The life cycle and net radiative effect of tropical anvil clouds. J. Adv. Model. Earth Syst., 10, 3012–3029, https://doi.org/ 10.1029/2018MS001484.
- ——, P. N. Blossey, and B. D. Dygert, 2019: Convection and climate: What have we learned from simple models and simplified settings? *Curr. Climate Change Rep.*, 5, 196–206, https://doi.org/10.1007/s40641-019-00136-9.
- Hersbach, H., and Coauthors, 2020: The ERA5 global reanalysis. *Quart. J. Roy. Meteor. Soc.*, **146**, 1999–2049, https://doi.org/10.1002/qj.3803.
- Holloway, C. E., and J. D. Neelin, 2007: The convective cold top and quasi equilibrium. J. Atmos. Sci., 64, 1467–1487, https:// doi.org/10.1175/JAS3907.1.
- Holton, J. R., P. H. Haynes, M. E. McIntyre, A. R. Douglass, R. B. Rood, and L. Pfister, 1995: Stratosphere-troposphere exchange. Rev. Geophys., 33, 403–439, https://doi.org/10.1029/ 95RG02097.
- Iacono, M. J., J. S. Delamere, E. J. Mlawer, M. W. Shephard, S. A. Clough, and W. D. Collins, 2008: Radiative forcing by long-lived greenhouse gases: Calculations with the AER radiative transfer models. J. Geophys. Res., 113, D13103, https://doi.org/10.1029/2008JD009944.
- Jucker, M., and E. P. Gerber, 2017: Untangling the annual cycle of the tropical tropopause layer with an idealized moist model. *J. Climate*, 30, 7339–7358, https://doi.org/10.1175/JCLI-D-17-0127.1.
- Khairoutdinov, M. F., and D. A. Randall, 2003: Cloud resolving modeling of the ARM summer 1997 IOP: Model

- formulation, results, uncertainties, and sensitivities. *J. Atmos. Sci.*, **60**, 607–625, https://doi.org/10.1175/1520-0469(2003) 060<0607:CRMOTA>2.0.CO;2.
- Kobayashi, C., and T. Iwasaki, 2016: Brewer-Dobson circulation diagnosed from JRA-55. J. Geophys. Res. Atmos., 121, 1493– 1510, https://doi.org/10.1002/2015JD023476.
- Kuang, Z., and C. S. Bretherton, 2004: Convective influence on the heat balance of the tropical tropopause layer: A cloudresolving model study. J. Atmos. Sci., 61, 2919–2927, https:// doi.org/10.1175/JAS-3306.1.
- Kubokawa, H., M. Fujiwara, T. Nasuno, M. Miura, M. K. Yamamoto, and M. Satoh, 2012: Analysis of the tropical tropopause layer using the Nonhydrostatic Icosahedral Atmospheric Model (NICAM): 2. An experiment under the atmospheric conditions of December 2006 to January 2007. J. Geophys. Res., 117, D17114, https://doi.org/10.1029/2012JD017737.
- Küpper, C., J. Thuburn, G. C. Craig, and T. Birner, 2004: Mass and water transport into the tropical stratosphere: A cloudresolving simulation. J. Geophys. Res., 109, D10111, https:// doi.org/10.1029/2004JD004541.
- Lin, P., D. Paynter, Y. Ming, and V. Ramaswamy, 2017: Changes of the tropical tropopause layer under global warming. *J. Climate*, 30, 1245–1258, https://doi.org/10.1175/JCLI-D-16-0457.1.
- Ming, A., A. C. Maycock, P. Hitchcock, and P. Haynes, 2017: The radiative role of ozone and water vapour in the annual temperature cycle in the tropical tropopause layer. *Atmos. Chem. Phys.*, 17, 5677–5701, https://doi.org/10.5194/acp-17-5677-2017.
- Morrison, H., J. A. Curry, and V. I. Khvorostyanov, 2005: A new double-moment microphysics parameterization for application in cloud and climate models. Part I: Description. *J. Atmos. Sci.*, 62, 1665–1677, https://doi.org/10.1175/JAS3446.1.
- Mote, P. W., and Coauthors, 1996: An atmospheric tape recorder: The imprint of tropical tropopause temperatures on stratospheric water vapor. *J. Geophys. Res.*, 101, 3989–4006, https://doi.org/10.1029/95JD03422.
- Powell, S. W., R. A. Houze, A. Kumar, and S. A. McFarlane, 2012: Comparison of simulated and observed continental tropical anvil clouds and their radiative heating profiles. *J. Atmos. Sci.*, **69**, 2662–2681, https://doi.org/10.1175/JAS-D-11-0251.1.

- Randel, W. J., and E. J. Jensen, 2013: Physical processes in the tropical tropopause layer and their roles in a changing climate. *Nat. Geosci.*, 6, 169–176, https://doi.org/10.1038/ngeo1733.
- —, and M. Park, 2019: Diagnosing observed stratospheric water vapor relationships to the cold point tropical tropopause. J. Geophys. Res. Atmos., 124, 7018–7033, https://doi.org/ 10.1029/2019JD030648.
- Robinson, F. J., and S. C. Sherwood, 2006: Modeling the impact of convective entrainment on the tropical tropopause. *J. Atmos. Sci.*, **63**, 1013–1027, https://doi.org/10.1175/JAS3673.1.
- Sherwood, S. C., T. Horinouchi, and H. A. Zeleznik, 2003: Convective impact on temperatures observed near the tropical tropopause. *J. Atmos. Sci.*, **60**, 1847–1856, https://doi.org/10.1175/1520-0469(2003)060<1847:CIOTON>2.0.CO;2.
- Stevens, B., and Coauthors, 2019: DYAMOND: The Dynamics of the Atmospheric general circulation Modeled on Nonhydrostatic Domains. *Prog. Earth Planet. Sci.*, 6, 61, https:// doi.org/10.1186/s40645-019-0304-z.
- Thompson, G., P. R. Field, R. M. Rasmussen, and W. D. Hall, 2008: Explicit forecasts of winter precipitation using an improved bulk microphysics scheme. Part II: Implementation of a new snow parameterization. *Mon. Wea. Rev.*, **136**, 5095–5115, https://doi.org/10.1175/2008MWR2387.1.
- Thuburn, J., and G. C. Craig, 2002: On the temperature structure of the tropical substratosphere. *J. Geophys. Res.*, **107**, 4017, https://doi.org/10.1029/2001JD000448.
- Voigt, A., N. Albern, and G. Papavasileiou, 2019: The atmospheric pathway of the cloud-radiative impact on the circulation response to global warming: Important and uncertain. *J. Climate*, 32, 3051–3067, https://doi.org/10.1175/JCLI-D-18-0810.1.
- Yang, Q., Q. Fu, J. Austin, A. Gettelman, F. Li, and H. Vömel, 2008: Observationally derived and general circulation model simulated tropical stratospheric upward mass fluxes. *J. Geophys. Res.*, 113, D00B07, https://doi.org/10.1029/2008JD009945.
- Yoshida, K., R. Mizuta, and O. Arakawa, 2018: Intermodel differences in upwelling in the tropical tropopause layer among CMIP5 models. *J. Geophys. Res. Atmos.*, **123**, 13 658–13 675, https://doi.org/10.1029/2018JD029044.
- Yulaeva, E., J. R. Holton, and J. M. Wallace, 1994: On the cause of the annual cycle in tropical lower-stratospheric temperatures. *J. Atmos. Sci.*, **51**, 169–174, https://doi.org/10.1175/1520-0469(1994)051<0169:OTCOTA>2.0.CO;2.